applied sciences

MDPI

Article

Receive/Transmit Aperture Selection for 3D Ultrasound Imaging with a 2D Matrix Transducer

Moein Mozaffarzadeh [1,*,†], Mehdi Soozande [2,†], Fabian Fool [1], Michiel A. P. Pertijs [3], Hendrik J. Vos [1,2], Martin D. Verweij [1,2], Johan G. Bosch [2] and Nico de Jong [1,2]

1 Laboratory of Medical Imaging, Department of Imaging Physics, Delft University of Technology, 2628 CJ Delft, The Netherlands; F.Fool@tudelft.nl (F.F.); h.vos@erasmusmc.nl (H.J.V.); M.D.Verweij@tudelft.nl (M.D.V.); Nicolaas.deJong@tudelft.nl (N.d.J.)

2 Department Biomedical Engineering, Thoraxcenter, Erasmus Medical Center, 3015 GD Rotterdam, The Netherlands; m.soozande@erasmusmc.nl (M.S.); j.bosch@erasmusmc.nl (J.G.B.)

3 Electronic Instrumentation Laboratory, Delft University of Technology, 2628 CD Delft, The Netherlands; M.A.P.Pertijs@tudelft.nl

* Correspondence: M.Mozaffarzadeh@tudelft.nl; Tel.: +31-06-1767-3356

† These authors contributed equally to this paper.

Received: 26 June 2020; Accepted: 29 July 2020; Published: 31 July 2020

Abstract: Recently, we realized a prototype matrix transducer consisting of 48 rows of 80 elements on top of a tiled set of Application Specific Integrated Circuits (ASICs) implementing a row-level control connecting one transmit/receive channel to an arbitrary subset of elements per row. A fully sampled array data acquisition is implemented by a column-by-column (CBC) imaging scheme (80 transmit-receive shots) which achieves 250 volumes/second (V/s) at a pulse repetition frequency of 20 kHz. However, for several clinical applications such as carotid pulse wave imaging (CPWI), a volume rate of 1000 per second is needed. This allows only 20 transmit-receive shots per 3D image. In this study, we propose a shifting aperture scheme and investigate the effects of receive/transmit aperture size and aperture shifting step in the elevation direction. The row-level circuit is used to interconnect elements of a receive aperture in the elevation (row) direction. An angular weighting method is used to suppress the grating lobes caused by the enlargement of the effective elevation pitch of the array, as a result of element interconnection in the elevation direction. The effective aperture size, level of grating lobes, and resolution/sidelobes are used to select suitable reception/transmission parameters. Based on our assessment, the proposed imaging sequence is a full transmission (all 80 elements excited at the same time), a receive aperture size of 5 and an aperture shifting step of 3. Numerical results obtained at depths of 10, 15, and 20 mm show that, compared to the fully sampled array, the 1000 V/s is achieved at the expense of, on average, about two times wider point spread function and 4 dB higher clutter level. The resulting grating lobes were at −27 dB. The proposed imaging sequence can be used for carotid pulse wave imaging to generate an informative 3D arterial stiffness map, for cardiovascular disease assessment.

Keywords: 3D ultrasound imaging; carotid pulse wave imaging; high frame rate; 2D matrix array; grating lobes reduction

1. Introduction

Arteriosclerosis is a very common cause of death worldwide, caused by deposition of lipids in the vessel wall in the form of plaques [1]. The relation between arterial stiffness and cardiovascular risk has been investigated in several studies as advanced arteriosclerosis can occlude arteries and involve changes of the vessel wall that reduce its elasticity and flexibility [2–4]. Estimation of the arterial stiffness

would be of significant interest because it provides valuable information for diagnosis, prognosis, and therapy of a patient [5]. Among all the methods to quantify arterial stiffness, the European Society of Cardiology has recommended to use the carotid-femoral pulse wave velocity (PWV) as a favored measure of aortic stiffness [5]. However, this is a global measure of arterial stiffness, in which local plaque stiffness plays no role. Assessment of arterial stiffness by imaging the local propagation of pulse waves can identify plaque characteristics, especially in the carotid arteries [6–8], which are prone to plaque development associated with stroke [9].

Pulse wave imaging (PWI) is usually conducted based on two-dimensional (2D) images of the pulse wave propagation [10–12]. However, it is a 3D phenomenon, and elasticity of the carotid artery varies in different locations [6,13]. Consequently, 2D images impose limitations. First, 2D elastography is sensitive to out-of-plane motion of the object, which can occur in carotid imaging [14]. Moreover, with conventional 2D ultrasound imaging, it is assumed that the propagation of the pulse wave is parallel to the imaging plane, which results in inaccuracies in PWV estimation [13]. A 3D assessment could be based on multiple cross-sectional 2D images of the 3D vessel structure, but it requires reproduction of the same imaging planes at later times, which is difficult [15]. Thus, it would be of great importance to have a comprehensive view of the arterial walls and generate a 3D elasticity map [13].

Going from 2D to 3D ultrasound imaging is challenging, and specific limitations are imposed, depending on the application [16,17]. One approach is to mechanically sweep the conventional one-dimensional (1D) linear or phased array probes (used in 2D imaging) by a motorized system to acquire a 3D dataset [18–20]. With this approach, a low volume rate along with large errors due to motion artifacts is obtained. Free-hand scanning techniques, in which a position and orientation sensor is added to the conventional 1D array transducer to record the trajectory and orientation, can be used to address the motion artifacts [18,21,22]. Still, a poor out-of-plane spatial resolution and a low volume rate limit the use of the mechanical scanning approach for applications such as echocardiography, where motion needs to be accurately tracked [15].

Another approach for 3D imaging is to make a 2D matrix array [23]. With a 2D array, the transducer can remain stationary, and electronic scanning can be used to sweep the ultrasound beam over the entire volume under examination [15], which can overcome the frame rate limitation. However, the fabrication and implementation of 2D matrix transducers are challenging. A large 2D transducer is required to obtain a high elevation and azimuth resolution. On the other hand, the element pitch should preferably be kept below half a wavelength (λ) in both directions to avoid grating lobes [24]. The combination of small elements and a large aperture results in a very large number of transducer elements. It is fairly possible to make a matrix array with >1000 elements, but making electrical connections to all the elements is challenging [25].

To realize a fully populated matrix transducer that uses a reduced number of channels, different approaches have been proposed. The signals from the elements in an aperture can be locally beamformed to obtain one output receive signal [26–29]. With the row-column addressed array approach, the number of channels required is reduced from N^2 to 2N, where N is the number of elements in each direction of a square matrix array, at the cost of image contrast and resolution [30–32]. Channel multiplexing is another approach to combine the data from several receive elements into one output line, at the cost of frame rate reduction [33].

We previously designed and manufactured a matrix transducer by fabricating an array of piezoelectric elements directly on top of an Application Specific Integrated Circuit (ASIC) [34]. A single tile of 12 × 40 (rows × columns) elements was developed as a building block for a larger transducer. The ASIC provides element-level switches and control logic which allow us to connect each individual element in a row (elevation direction) to a corresponding row-level transmit/receive bus. In this study, we use a 4 × 2 tiles configuration to form a large transducer consisting of 48 × 80 (azimuth × elevation) elements. Based on the transducer architecture, 80 transmit/receive shots are required to fully read out the element data for a single plane wave imaging. Considering a pulse repetition frequency (PRF) of 20 kHz (for a depth of 37.5 mm deep enough for carotid PWI (CPWI) [8]), a volume rate of 250 per

second can be achieved. However, for CPWI, 1000 V/s are needed [8,35,36]. Therefore, we are obligated to limit the number of receive/transmit shots to 20. To do so, in this paper, we propose to interconnect elements into non-delayed apertures which can be shifted in the elevation direction. We investigate the effects of receive and transmit aperture sizes and aperture shifting step in numerical simulations and in an in vitro experimental setup. An angular weighting (AW) method (based on the directivity pattern of the receive apertures) is used in the image reconstruction procedure to reduce the effects of grating lobes (caused by the increased effective pitch in elevation direction). The goal is to find a trade-off to form good-quality B-mode images, providing suitable inputs for motion estimation methods used in wall velocity measurement [8,13].

2. Materials and Methods

2.1. Imaging Schemes

For CPWI, the lateral direction in our 2D assessment (the elevation direction in 3D imaging) lies perpendicular to the carotid artery. For people of age over 60 years, the carotid diameter is 7.4 ± 0.7 mm and 8.2 ± 0.8 mm and over 70, it is 7.6 ± 0.8 mm and 9 ± 0.7 mm, for females and males, respectively [37]. The effective covered aperture size is calculated as (Nr + 19Ns) × Pitch, where Nr is the receive aperture size, Ns is the shift of the receiving aperture between sequential shots, and Nt is transmit aperture size. With Ns 1 and 2 and with a small Nr, the obtained effective aperture is much less than what is needed to cover the whole carotid artery. As we aim to have an effective covered aperture size big enough for all ages, we neglect Ns of 1 and 2 in our study.

A tile of 12 × 40 elements (rows × columns) requires 12 channels for transmission and 12 channels for data reception (Figure 1a). The row-level circuitry allows us to put two tiles head-to-head in a row to form an array of 12 × 80 elements without increasing the channel count [33]. In this study, the array is fabricated using 4 × 2 (rows × columns) tiles providing 48 × 80 (azimuth × elevation) elements (Figure 1b; the carotid has a diameter of 6–9 mm [37]; the array is 14 × 12 mm). A single plane wave imaging with full data acquisition can be implemented using a column-by-column (CBC) data acquisition approach which requires 80 transmit/receive shots. In this approach, all the 80 elements are connected to the transmit bus, and only a single element in the elevation direction is connected to the receive bus. For CPWI, we need 1000 V/s which restricts the number of transmit-receive shots to 20 for one volume. These 20 shots can be implemented in different manners; an example is shown in Figure 2b where the transmit aperture of 50 elements is shifted over three elements for each step, co-aligned with the receive aperture of 10 elements.

Applying dynamic focusing to the received data having an effective element pitch larger than half of a wave length introduces grating lobes [24]. In our study, the 2D matrix transducer has an elevation pitch of 150 µm, and the operating frequency ranges from 6 to 9 MHz, i.e., the shortest wavelength is 170 µm in tissue. Therefore, grating lobes in the elevation direction will appear.

The current ASIC architecture can accommodate 20 arbitrary transmit/receive patterns in the provided memories, which can be used to define sparse patterns (out of the scope of this paper) [34]. In addition to these element level memories, elements can be grouped into a set of transmit/receive apertures with an arbitrary size and shifted along elevation direction with one element per clock cycle [34]. In this study, we use this feature to define regular aperture patterns (see Figure 2b for example). The elements contributing in a receive aperture are interconnected (switched in parallel without further inter-element delays) in practice, and one time series is achieved for the receive aperture.

2.2. Numerical Studies on the Beam Profile

As element interconnection only happens in the elevation direction, our numerical evaluation was only conducted in the elevation direction. Simulations were conducted in Field II [38,39] to investigate the beam profile of the different transmit/receive sequences. The image reconstruction in azimuthal direction is unaffected and therefore neglected. We varied the settings provided in Table 1.

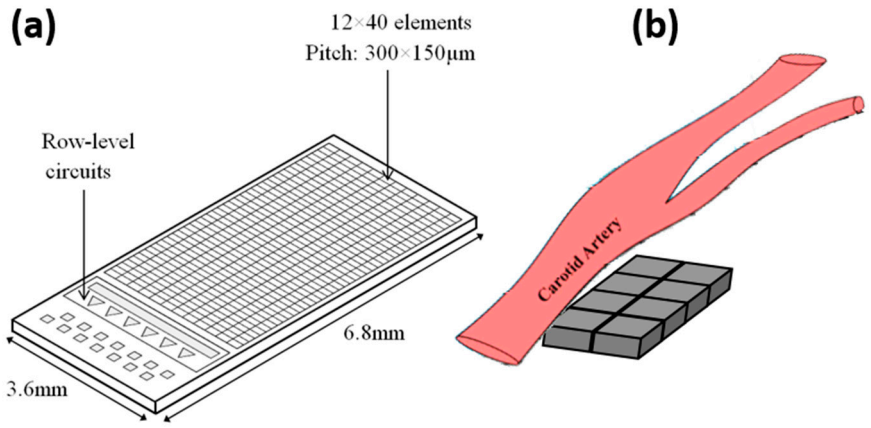

Figure 1. (**a**) Schematic of a single tile consisting of 12 × 40 acoustic elements on top of an Application Specific Integrated Circuit (ASIC) with element-level switches and row-level circuits. (**b**) The proposed transducer consisting of 4 × 2 tiles with respect to the carotid artery (carotid has a diameter of 6–9 mm; the array is 12 × 14 mm).

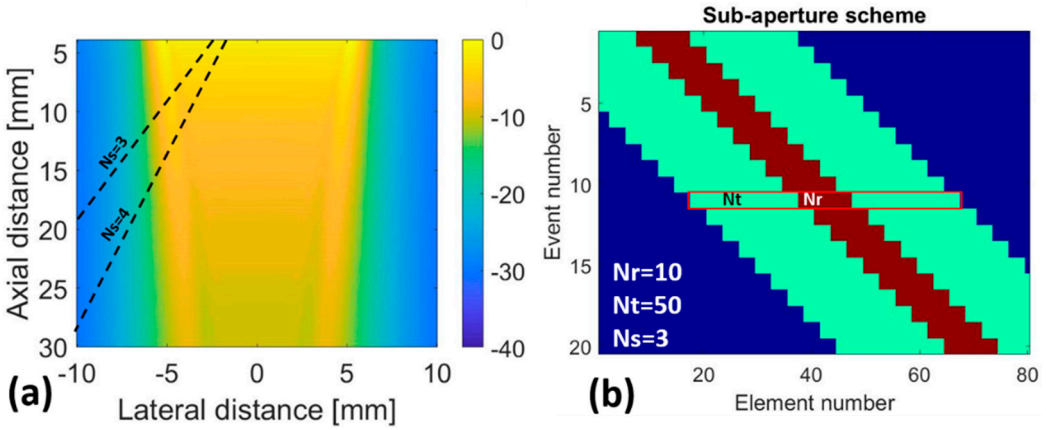

Figure 2. (**a**) The generated pressure field with a full transmission approach (all the elements are excited together); the dashed lines show the direction of grating lobes with different Ns. (**b**) A schematic of the aperture definition procedure; Ns = 3, Nr = 10, and Nt = 50. Receive and transmit apertures have the same center.

Table 1. The variables used in the numerical study.

Number of Shots	**20**
Receive aperture (Nr)	1–20 elements
Element size	130 μm
Pitch	150 μm
Transmit aperture	1–80 elements
Shift between sequential shots of the receive aperture (Ns)	3–4 (unit is Pitch)
Transmit pulse length	1.5 cycles
Central frequency	7.5 MHz, λ = 0.2 mm
Scatterer position	10, 20, and 30 mm
Speed of sound	1500 m/s
Sampling frequency	100 MHz

The impulse response consisted of a Gaussian-modulated sinusoidal waveform (central frequency of 7.5 MHz, bandwidth of 80%). Normalization and log-compression were used to form final images. The response of receive aperture size (Nr), the shift of the receiving aperture between sequential shots

(Ns) and the transmit aperture size (Nt) were evaluated using point scatterers positioned at depths of 10, 15, and 20 mm, as we expect the carotid artery in this range [8]. Figure 2b illustrates the way that the Nr, Nt, and Ns parameters were defined and implemented in 20 transmit-receive shots. The receive and transmit apertures were concentric and shifted over the same distance.

The level of grating lobes, lateral width of point spread function (PSF) at −6 dB called full-width-half-maximum (FWHM) and level of sidelobes were used to evaluate the image quality as result of the different settings [24]. The finalized imaging sequence was evaluated with a numerical tissue mimicking phantom in which an anechoic cyst having a radius of 3 mm was positioned at the depth of 15 mm. The phantom contained scatterers from −15 to 15 mm in the lateral direction to visualize the off beam energy including the grating lobes. Multi-scatterer and multi-cyst phantoms were also imaged. We use column-by-column imaging scheme as the ground truth (GT) in our study.

2.3. Experimental Study

The 2D matrix array was mounted in a box with an acoustically transparent window (25 µm thick polyimide) and the whole setup was submerged in a tank filled with water (see Figure 3a). The transducer was excited by a custom-programmed experimental ultrasound system (Vantage 256, Verasonics, Kirkland, WA, USA). A picture of the two-needle phantom used in our experiments is provided in Figure 3d. The axial distance between the plastic foam, that acts as base to the needles, and the surface of our 2D transducer was about 26 mm. Matlab 2018b and MeVisLab (MeVis Medical Solutions AG, Fraunhofer MEVIS, Bremen, Germany) software was used to process the data and show 3D images, respectively.

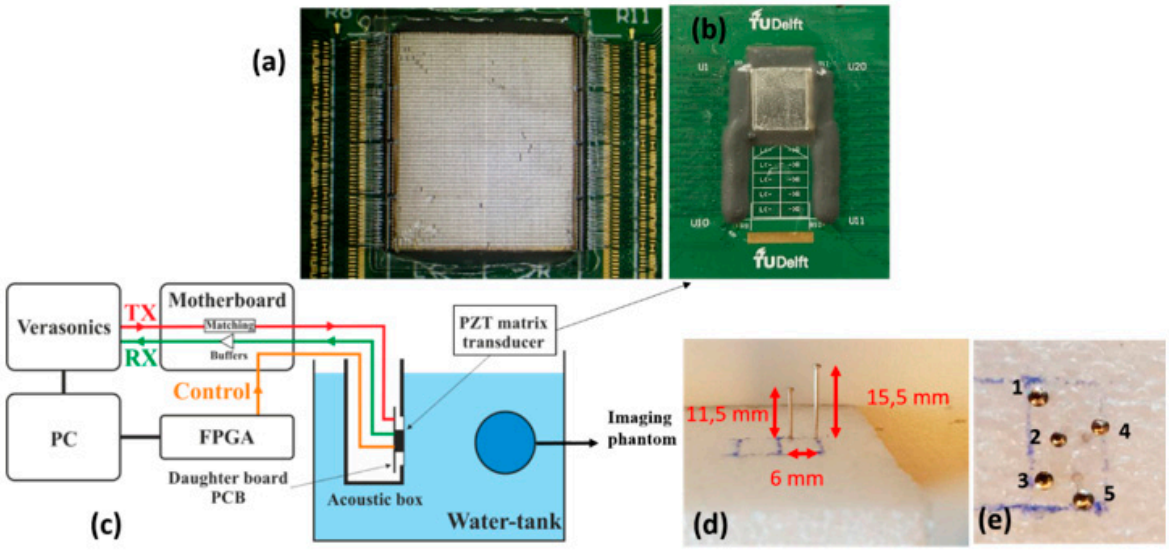

Figure 3. (**a**) The daughterboard with the transducer array before applying the ground foil. (**b**) The finalized 4 × 2 matrix array. (**c**) Schematic of the measurement setup. (**d**) The imaging phantom: a foam pad with two needles. The distance between the foam and the transducer surface is about 26 mm. (**e**) The imaging phantom: a foam pad with five needles, positioned in different depths (from 10 to 20 mm). The distance between the foam and the transducer surface is about 28 mm. The numbers next to the needles are used for target localization in Section 3.

3. Results

3.1. Numerical Results: Point Scatterer

3.1.1. Receive Aperture

Figure 4a,b shows the PSF for varying receive aperture (Nr) between 1 and 20 elements and shifting steps (Ns) of 3 and 4. A full-aperture transmission (transmission with all the elements) is

used (Nt = 80) and 20 shots are given. For a receive aperture equal to one element (Nr = 1) and step size of three elements (Ns = 3), the total covered aperture is 8.7 mm resulting in a main beam width of about 2 mm at 10 mm distance. The grating lobe level is −20 dB as expected from the 1.5 cycle excitation and 20 shots and positioned at a lateral distance of −5 mm caused by the large step (Ns = 3, effective pitch = 450 μm, λ = 200 μm). The mean beam width remains about the same for larger Nr up to 5 (see Figure 4e) since two opposite effects play a role. The first one is the slowly increasing covered aperture (e.g., for Nr = 5, the covered aperture is 9.3 mm). The opposite one is the increasing directivity of the receiving apertures (for Nr = 5 the directivity is about 10°), which makes the contribution of the outer elements less. For larger receive apertures, Nr = 10 the main beam width is increased to about 3 mm and it further increases to 4.2 mm for Nr = 20. For Nr = 20, the covered aperture is admittedly the largest, but very directive (2°), and therefore only the middle part of the covered aperture is contributing in image reconstruction. For Ns = 4 (see Figure 4b), the grating becomes stronger, making the grating lobes appear closer to the mainlobe, at −4 mm lateral distance (see the rectangles in Figure 4a,b).

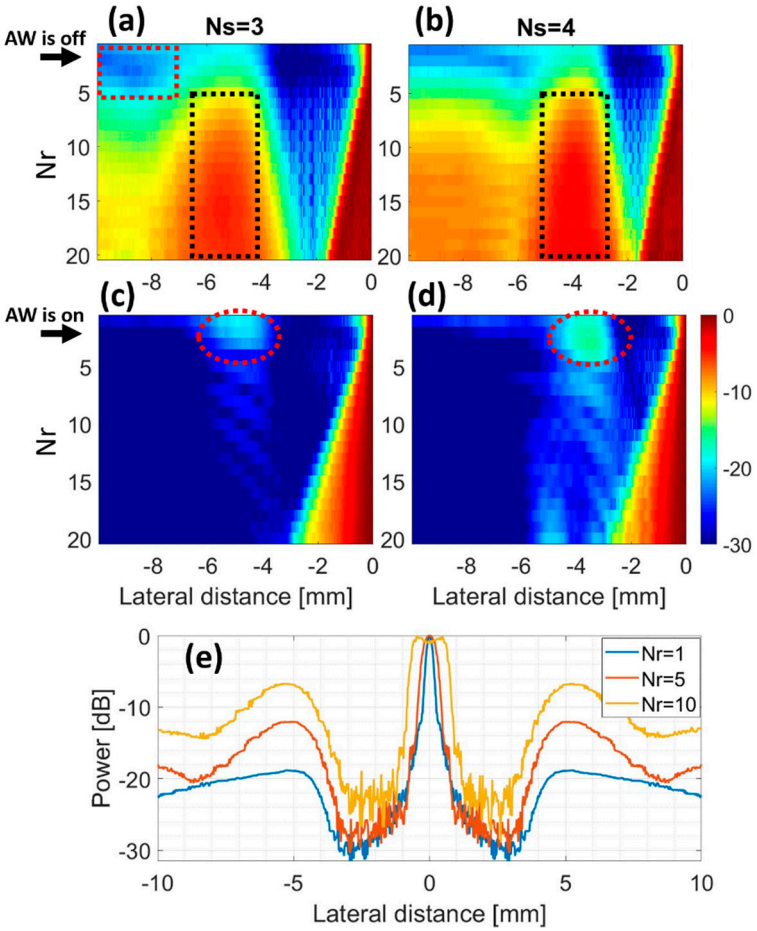

Figure 4. (**a**–**d**) The point spread functions (PSFs) obtained for different Nr and Ns when a full-aperture transmission is used. A point scatterer was positioned at the depth of 10 mm and the lateral distance of 0 mm. The angular weighting (AW) technique was used in the bottom row. The black and red rectangular regions were used to calculate the clutter level (Figure 5a) and effects of grating lobes (Figure 5b). The red circles show the effects of grating lobes. (**e**) The lateral variation for Ns = 3 when the AW is on.

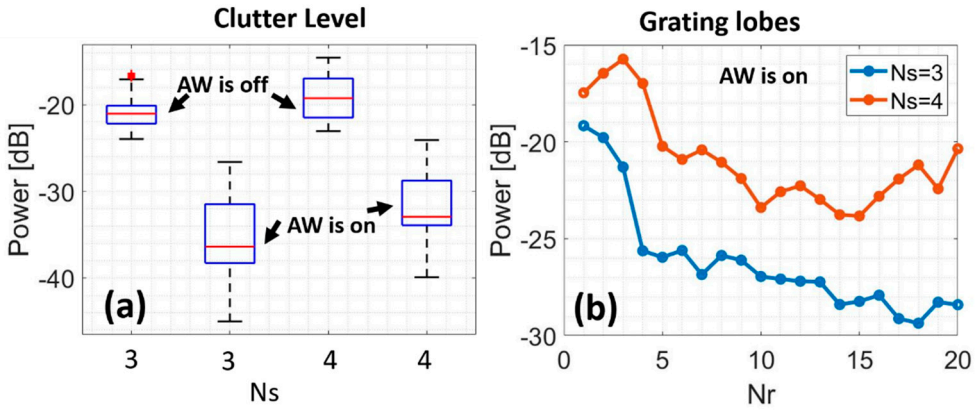

Figure 5. (**a**) Distribution of clutter level measured within the red rectangular region shown in Figure 4a. The same area was used in other images. On each box, the central mark indicates the median of the clutter level inside the corresponding region. The bottom and top edges of the box indicate the 25th and 75th percentiles, respectively. The whiskers extend to the most extreme data points not considered outliers. Outliers were plotted individually using the '+' symbol. (**b**) The level of grating lobes, measured within the black rectangular regions indicated in Figure 4.

Since the effective aperture can be very large and directive, angular weighting, as described in [40], can be applied in reception. This results in reduced grating lobes (compare the first and second rows in Figure 4) and about 16 and 13 dB lower clutter level for Ns of 3 and 4, respectively (see Figure 5a where the pixel intensities within the red rectangular regions shown in Figure 4a were used for statistical analysis). The level of grating lobes (for different Nr) obtained with the AW technique is presented in Figure 5b. The AW technique hardly works for Nr of 1 up to 5 due to the large angular view of the receive aperture.

Figure 6 shows the FWHM as function of aperture settings. It indicates that the smaller the Nr, the lower the FWHM (i.e., better lateral resolution). This is mainly because we use the dynamic focusing technique in reception, and increment in Nr results in a narrower directivity in each receive aperture, which reduces the effective number of elements (i.e., aperture size) contributing in the reconstruction of a given pixel (voxel in 3D).

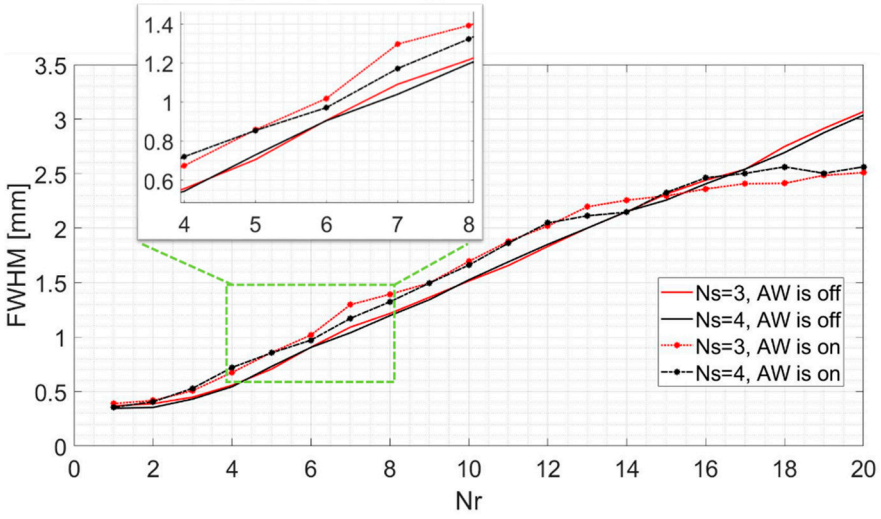

Figure 6. Full-width-half-maximum (FWHM) measurements for different Nr and Ns; a full-aperture transmission was used.

An analysis of Figures 4 and 6 shows that the AW technique helps with suppression of the grating lobes at the expense of resolution. With an AW, a higher contrast can be expected [40], helping the

motion estimation methods used to estimate the wall velocities in CPWI [8]. Thus, we use AW technique in the reconstruction through rest of the paper.

As seen in Figure 4c,d, grating lobes are not well-suppressed for Nr = 1 (see the red circles). For Ns = 3, these effects reduce about 6 dB from Nr = 1 to Nr = 5 and then reduce with a lower rate along with oscillation (see Figures 4c and 5b). Almost the same pattern happens for Ns = 4 from Nr = 1 to Nr = 5. We also noticed the same trend happening at depths of 15 and 20 mm (depths of interest for CPWI [8])—results are not provided here. Based on the lower grating lobes for Ns = 3 than Ns = 4 (Figure 5b), the reduction of grating lobes from Nr of 1 to 5 for Ns = 3 (Figure 5b), and the same resolution in Nr = 5 for Ns of 3 and 4 (see zoomed version in Figure 6), we proceed with Ns = 3 and Nr = 5. It is true that Nr = 5 increases the FWHM more than a smaller Nr (see Figure 6), but lower grating lobes are more beneficial/needed in CPWI than a higher resolution due to motion estimation algorithms used in CPWI [8,13]. Although even lower grating lobes can be achieved by a Nr larger than 5 (Figure 5b), the rate of FWHM increment is much larger than the rate of grating lobes decrement (see Figure 6) when Nr increases. It is expected to have 7 dB higher signal-to-noise ratio (SNR) with Nr = 5 than Nr = 1. Moreover, with Ns = 3 and Nr = 5, an effective covered aperture of 9.3 mm can be obtained, which is large enough to cover the carotid artery in all ages [37].

We conducted the same assessment for scatterers positioned at depths of 15 and 20 mm (results not shown). For different Ns, almost the same difference in the mean of the level of grating lobes (red lines in Figure 6a) is achieved. The same effects indicated by the red circles Figure 4c,d occur, but with lower power. Following the same procedure Ns = 3 and Nr = 5 can be selected for receive aperture in these depths as well.

3.1.2. Transmit Aperture

So far, we used a full-aperture transmission. In this section, we evaluate the effects of the transmit aperture size (Nt) on the PSFs obtained with the selected reception parameters (Nr = 5 and Ns = 3). Figure 7a–c shows the PSFs obtained with different Nt while a scatterer is positioned at the depths of 10, 15, and 20 mm, respectively. A small Nt leads to strong artifacts caused by the grating lobes. This is due to the omnidirectional pressure field in transmission which causes excitation in the direction of the grating lobes with the same energy as that of main lobe. As the Nt gets larger, the transmission pressure field gets more directional toward the front side of the array and becomes like what is shown in Figure 2a. In higher depths, the effects of grating lobes are lower since a lower pressure is transmitted in the direction of the grating lobes (see Figure 2a).

The effects of grating lobes are lower when Nt is larger than 20 (see Figure 7a–c). From Nt of 1 to 50 the FWHM decreases, and reaches an asymptotic minimum for Nt larger than 50. However, around a Nt of 50, the effects of sidelobes are still more powerful than larger Nt (compare the regions shown by the red and green dashed rectangles in Figure 7a–c). Since the larger the Nt, the lower the effects of sidelobes, we proceed with a full-aperture transmission (Nt = 80).

3.1.3. Lateral Shift Variance

In Figure 7d,e, point scatterers positioned at the depths of 10 and 20 mm, respectively, are laterally shifted from −6.5 to 6.5 mm. This image is normalized to its maximum to fairly track the effects of grating lobes (see the green arrows) [41]. Figure 7d,e indicates that if a scatterer is positioned in the direction of the grating lobes, its effect is much lower than that of a scattering target in the middle of the array. This is mainly because of the AW technique in reception and the fact that the direct transmitted pressure field excites targets in the lateral center of the array with a higher power, compared to those in the grating lobes angles (see Figure 2a). The best resolution is also obtained when the scatterer is at the lateral center.

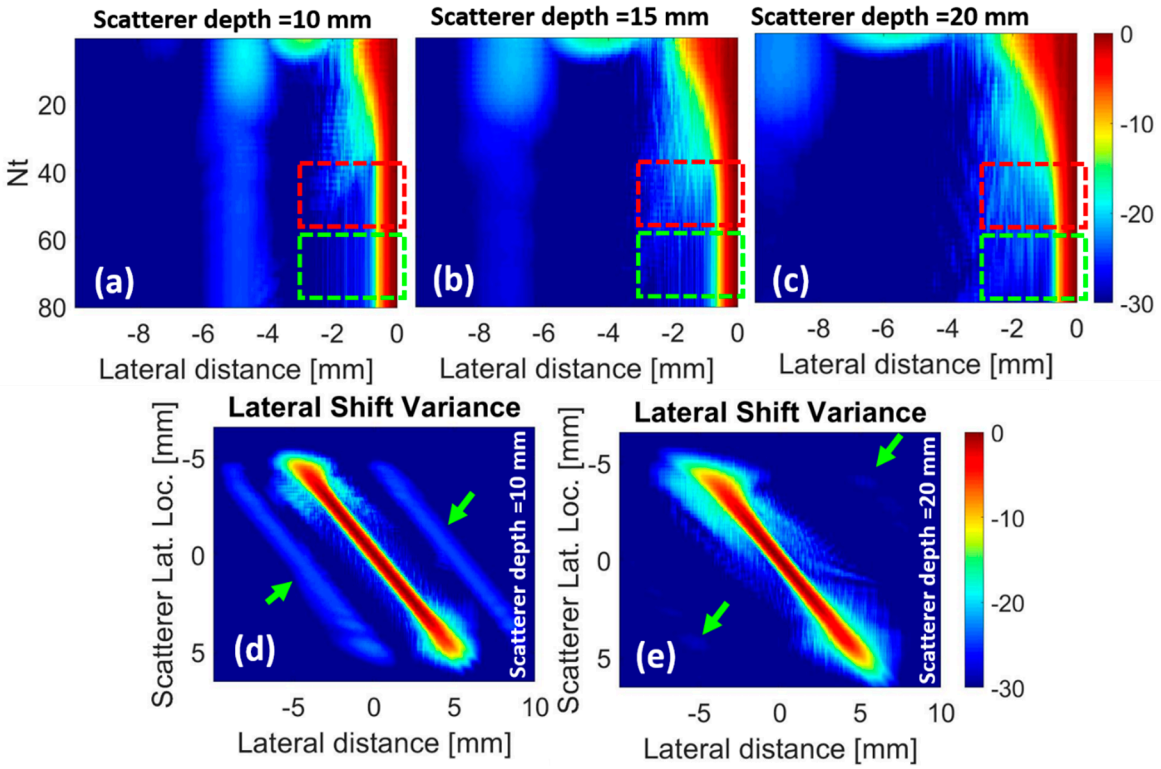

Figure 7. (**a**–**c**) The PSFs obtained for different Nt; Nr = 5, Ns = 3. The green rectangular regions show a reduction of sidelobes with respect to the red rectangles. (**d**,**e**) The lateral shift variance for full-aperture transmission, Nr = 5 and Ns = 3, for a scatter at a depth of (**d**) 10 mm and (**e**) 20 mm. Green arrows: location of grating lobes.

3.1.4. Comparison with Ground Truth

A comparison between the reconstructed images by the proposed imaging sequence (full-aperture transmission, Nr = 5 and Ns = 3) and the CBC imaging sequence (ground truth, GT) at three depths of interest is provided in Figure 8a,b, along with their corresponding PSFs in Figure 8c. The AW is applied to the GT to have a fair comparison. By the proposed imaging sequence, the FWHM is almost doubled due to the larger receiving aperture, and the mean clutter level, on average, is 4 dB higher than GT, with a level of grating lobes of about −24, −27, and −29 dB, at the depths of 10 mm, 15 mm, and 20 mm, respectively. See the Supplementary Materials (Figure S1) for the results obtained using the multi-scatterer phantom.

3.2. Numerical Results: Cysts Phantom

The results obtained with the cyst phantom are shown in Figure 9. The images are laterally limited due to the narrow transmission beam profile (see Figure 2a). The proposed scheme (Figure 9a) is more laterally limited because of the smaller effective aperture size than the CBC GT (Figure 9b). The red arrows in Figure 9a show the effects of grating lobes. To statistically compare these images, pixel intensities within two regions of interest (ROI1 and ROI2, the red and yellow circles in Figure 9b) are used. For the proposed imaging sequence, the mean of ROI1 is 6 dB higher than GT (see Figure 9c) due to the effects of the grating lobes and sidelobes (see Figure 8c). The 3 dB higher mean in ROI2 provided by the proposed imaging sequence (Figure 9c) is also due to the larger FWHM and more constructive interferences of the point scatterers. See the Supplementary Materials (Figure S2) for the results obtained using the multi-cyst phantom.

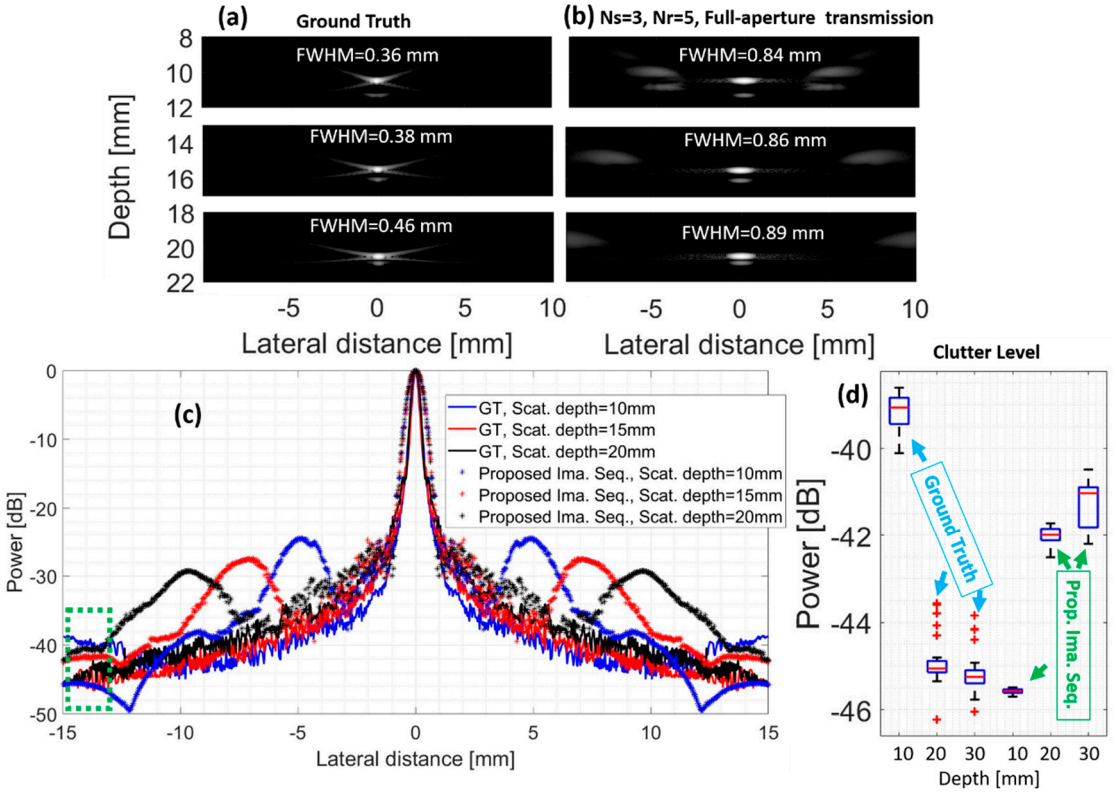

Figure 8. The reconstructed images using (**a**) the column-by-column (CBC) imaging sequence (ground truth—GT) and (**b**) the proposed imaging sequence (full-aperture transmission, Nr = 5 and Ns = 3), along with (**c**) their corresponding lateral variations. The AW is applied on the GT to have a fair comparison. (**d**) The clutter level using the green rectangular region in (c).

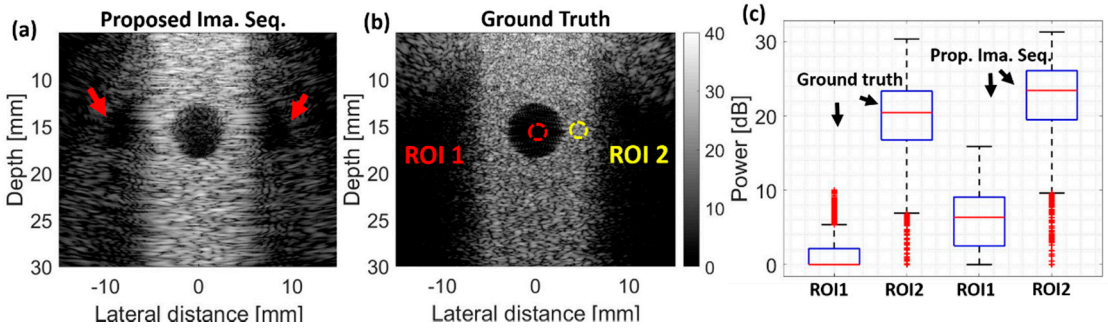

Figure 9. The reconstructed images using (**a**) the proposed imaging sequence (full-aperture transmission, Nr = 5 and Ns = 3) and (**b**) the CBC imaging sequence (GT). (**c**) Statistical analysis of the image intensities indicated by two regions of interest (ROI1 and ROI2) which are the red and yellow circles, respectively.

3.3. Experimental Results

Figure 10 presents the experimental results of the 3D reconstructed images using the GT and the proposed imaging sequence (full-aperture transmission, Nr = 5 and Ns = 3). The AW is applied on the GT to have a fair comparison. The red, yellow, green, and blue arrows show the foam, the two needles, the grating lobes, and the clutter in the azimuth direction, respectively. The smaller size of foam in Figure 10b,e is due to a smaller effective aperture size in the elevation direction. A better visualization on the needles is achieved in Figure 10e compared to Figure 10d due to the AW technique.

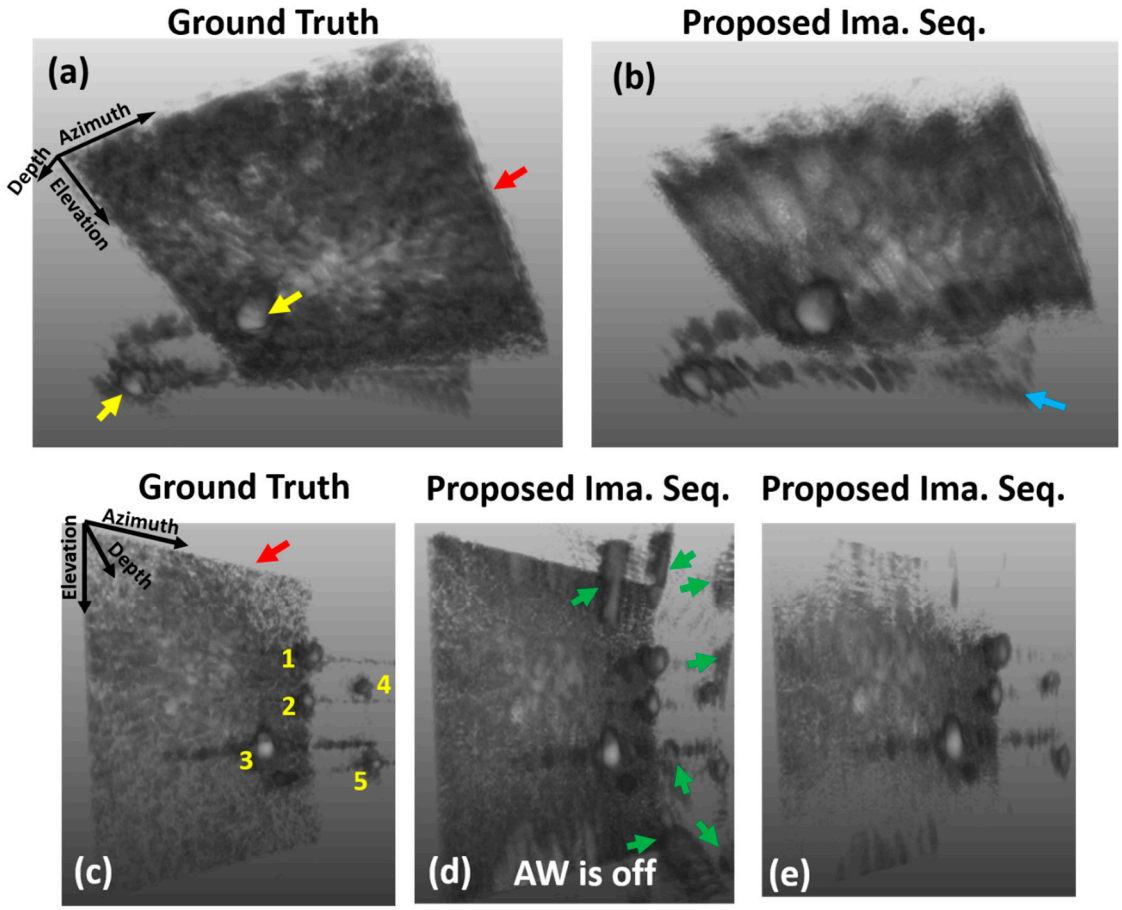

Figure 10. The 3D images obtained with (**a**,**c**) the CBC imaging sequence (GT) and (**b**,**d**,**e**) the proposed imaging sequence (full-aperture transmission, Nr = 5 and Ns = 3). The red, yellow, green, and blue arrows show the foam, the two needles, the grating lobes, and the clutter in the azimuth direction, respectively. The dynamic range was 40 dB. The numbers in (**c**) are related to those shown in Figure 3e.

The maximum intensity projection (MIP) over a depth of 1–23 mm of the 3D experimental images obtained with the two-needle phantom is shown in Figure 11a–c. The elevation FWHM obtained with the proposed imaging sequence at the depth of about 10 mm is doubled, in accordance with the results provided in Figure 8a,b. This is the reason that the targets look stretched in the elevation direction, as seen in Figures 11a and 10b. The azimuth FWHM for different receive parameters stays the same (about 620 μm) as the proposed imaging sequence does not significantly affect the performance of the 2D transducer in the azimuth direction. The same clutter patterns for different Ns, but the same Nr, also prove this matter (see Figure 11d). The clutter level in azimuth direction is higher than elevation direction due to the larger pitch (300 μm) and lower number of elements (48).

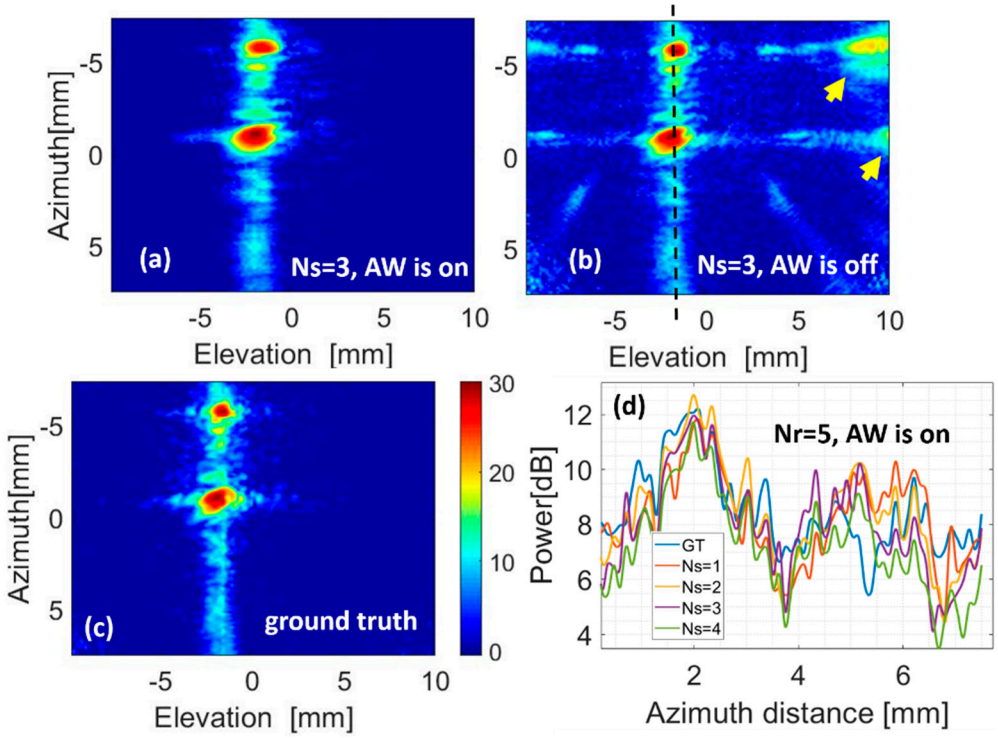

Figure 11. (**a**–**c**) The maximum intensity projection (MIP) of the reconstructed 3D images of Figure 10 using the data obtained with the two-needle phantom. (**d**) The clutter pattern in azimuth direction measured on the dashed black line in (**b**).

4. Discussion

The aim of this study was to find a set of imaging parameters that provides a good image quality using an aperture-shifting matrix array, within the boundary condition of a limited number of transmissions (20), such that a volume frame rate of 1000 per second could be reached. We aimed for such high volume rate to facilitate CPWI (seeing the 4.5 m/s pulse wave pass laterally within a few volumes [8]). Depths of evaluation were 10, 15, and 20 mm as the anterior and posterior walls are expected at these depths [8]. The effects of receive aperture size (Nr), the aperture shifting distance per pitch (Ns), and transmit aperture size (Nt) were studied.

Improving the quality of B-mode images helps in CPWI as it facilitates the motion estimation algorithms to track the axial displacement of the arterial walls [8,13]. This is essential for accurate local pulse wave velocity estimation required to generate an elasticity map. Our assessment and parameters selection priority were as follows: (1) the size of effective aperture; as it indicates whether we can have a comprehensive view on the carotid artery or not [37], (2) suppression of grating lobes; the lower the level of grating lobes, the higher the contrast, which is important for motion estimation algorithms to better estimate the axial displacement of carotid walls [8], and (3) resolution/sidelobes. Both Ns of 3 and 4 could provide sufficiently large effective aperture. Due to the lower grating lobes achieved with Ns = 3, compared to Ns = 4, Ns = 3 was selected. Selection of Nr imposed a trade-off between FWHM and grating lobes. The rate of decrement of grating lobes and increment of FWHM in Ns = 3 led to a Nr of 5. Almost the same trends happened in all the three depths of interest for CPWI [8], which led us to Ns = 3 and Nr = 5. The finalized imaging sequence, with a boundary condition of 20 transmit-receive shots, consists of a full-aperture transmission (Nt = 80), Nr = 5, Ns = 3 and using the angular weighting (AW) technique in the image reconstruction procedure.

Signal-to-noise ratio (SNR) is also an important criterion in the performance of motion estimation techniques. However, it is not included in our study since in previous studies, an acceptable SNR in CPWI was achievable with both 1D or 2D arrays [8,13], and it is expected that this is the case with our

2D matrix array as well [34]. If SNR is not good enough (either for CPWI or other applications which need the same effective aperture size) to perform a reliable motion estimation, a larger Nr can be used. However, it would cause a larger FWHM as a consequence of relatively more direct receive apertures and applying the dynamic focusing in reception. Therefore, in the case of using a large Nr (i.e., 20), a more sophisticated image reconstruction method, which takes the narrow directivity of a large Nr into account, should be used in the elevation direction to form a 3D volume [42].

The final version of our 2D transducer will have 10 tiles in the azimuth (row) direction and two tiles in the elevation (column) direction, making 120 × 80 (row × column) elements available to form a 3D image. Having an azimuth pitch of 300 µm, the size of our 2D transducer in azimuth direction will be 36 mm, thus providing an aperture size big enough to track the carotid pulse wave velocity (estimated to be around 4.5 m/s [8]). All the evaluations and decisions in this paper were conducted using static imaging phantoms while in CPWI, there are several types of motion, i.e., carotid wall movement caused by pulse wave propagation, overall movement by breathing, and patient/transducer movement. Motion of the object might lead to unwanted decorrelation of the signals recorded by the sequentially switched apertures, leading to lower image quality. To calculate the risk of such decorrelation, we performed the following calculation. The wall velocity is, estimated from the interframe axial displacement, reported to be about 5 mm/s [8,13]. Considering the 1 ms needed for data acquisition by the proposed imaging sequence for a 3D volume, the target moves 5 µm in the axial direction. In this scenario, the PSF obtained with a dynamic scatterer, moving 5 µm in 20 transmit-receive shots, well overlaps with a static scatterer, which is mainly because the motion is lower than 10% of the wavelength (200 µm) during the time needed to acquire the data of a 3D volume [43]. Therefore, we can assume that the coherent compounding from the 20 acquisitions is not negatively affected. In addition, the global movement is slow, will not interfere with the coherent image reconstruction, and can be removed by subtraction of displacement of the tissues and that of carotid artery [8].

With 20 kHz pulse repetition frequency, reflection artifacts come from depths higher than 37.5 mm. In this study, these reflection artifacts are ignored due to tissue attenuation (≈0.4–0.6 dB/MHz/cm) as a scatterer at a higher depth (e.g., 50 mm) is attenuated by 28 dB compared to the reflection coming from 12.5 mm depth. A more advanced beamforming algorithm might be helpful with suppression of these artifacts as well [44–47], taking the change of speckle patterns into account [48].

Finally, although the reported results are linked to the specifications of the matrix transducer reported in our previous publication (see [34]), we would like to stress that the procedure taken in this study to select receive/transmit parameters can be used for other array transducers (either 1D or 2D) to obtain a higher frame/volume rate at a given number of data acquisition channels.

As a future study, we will use the proposed imaging sequence to conduct clinical 3D carotid pulse wave imaging and generate 3D elasticity maps.

5. Conclusions

In this paper, we evaluated the effects of receive/transmit parameters on the image quality provided by a linear array in which elements are mutually interconnected, which mimics the elevation direction of our prototype 2D matrix transducer. The parameter selection procedure was based on the effective covered aperture size, level of grating lobes, and resolution/sidelobes. To achieve 1000 volumes/second, only 20 transmit-receive shots were available, considering a pulse repetition frequency of 20 kHz and imaging depth of 37.5 mm. To suppress the effects of grating lobes, an angular weighting technique was used. The proposed imaging sequence consisted of a full-aperture transmission (all 80 elements), receive aperture size of 5, and aperture shifting distance of three elements. For depths of 10–20 mm, the results show that, on average, about two times wider point spread function at −6 dB and marginally (4 dB) higher clutter level were obtained, compared to the ground truth, and grating lobes level of about −27 dB lower than the main lobe. Having a proper imaging sequence based on 1000 V/s could

be beneficial to generate 3D maps of carotid artery stiffness, providing valuable information regarding the cardiovascular risk.

Supplementary Materials: The following are available online at http://www.mdpi.com/2076-3417/10/15/5300/s1, The results obtained with multi-scatterer and multi-cyst phantoms are provided in the supplementary document.

Author Contributions: Conceptualization, M.M. and M.S.; methodology, M.M., M.S. and F.F.; formal analysis, M.A.P.P., H.J.V., M.D.V., J.G.B. and N.d.J.; investigation, M.M., M.S., J.G.B. and N.d.J.; resources, M.A.P.P., H.J.V., M.D.V., J.G.B. and N.d.J.; data curation, M.M., M.S. and F.F.; writing—original draft preparation, M.M. and M.S.; writing—review and editing, F.F., M.A.P.P., H.J.V., M.D.V., J.G.B. and N.d.J.; visualization, M.A.P.P., H.J.V., M.D.V., J.G.B. and N.d.J.; supervision, M.A.P.P., H.J.V., M.D.V., J.G.B. and N.d.J.; project administration, M.A.P.P., H.J.V., M.D.V., J.G.B. and N.d.J.; funding acquisition, M.A.P.P., H.J.V., M.D.V., J.G.B. and N.d.J. All authors have read and agreed to the published version of the manuscript.

Funding: This research is a part of the 3D-ICE, PUMA and UltraXtreme projects (project numbers 14297, 13154 and P17-32, respectively), which are partly financed by the Netherlands Organisation for Scientific Research (NWO). Moreover, the authors acknowledge a joint grant from the NWO/ the Netherlands Organisation for Health Research and Development (ZonMw) and the Department of Biotechnology (Government of India) under the program Medical Devices for Affordable Health (MDAH) as Project Imaging Needles (Grant Number 116310008).

Conflicts of Interest: The authors declare no conflict of interest.

References

1. Moon, H.D.; Rinehart, J.F. Histogenesis of Coronary Arteriosclerosis. *Circulation* **1952**, *6*, 481–488. [CrossRef]
2. Laurent, S.; Katsahian, S.; Fassot, C.; Tropeano, A.-I.; Gautier, I.; Laloux, B.; Boutouyrie, P. Aortic Stiffness Is an Independent Predictor of Fatal Stroke in Essential Hypertension. *Stroke* **2003**, *34*, 1203–1206. [CrossRef]
3. Laurent, S.; Boutouyrie, P.; Asmar, R.; Gautier, I.; Laloux, B.; Guize, L.; Ducimetiere, P.; Benetos, A. Aortic stiffness is an independent predictor of all-cause and cardiovascular mortality in hypertensive patients. *Hypertensions* **2001**, *37*, 1236–1241. [CrossRef]
4. Sutton-Tyrrell, K.; Najjar, S.S.; Boudreau, R.M.; Venkitachalam, L.; Kupelian, V.; Simonsick, E.M.; Havlik, R.; Lakatta, E.G.; Spurgeon, H.; Kritchevsky, S.B.; et al. Elevated Aortic Pulse Wave Velocity, a Marker of Arterial Stiffness, Predicts Cardiovascular Events in Well-Functioning Older Adults. *Circulation* **2005**, *111*, 3384–3390. [CrossRef]
5. Mancia, G.; De Backer, G.; Dominiczak, A.F.; Cífková, R.; Fagard, R.; Germano, G.; Grassi, G.; Heagerty, A.M.; Kjeldsen, S.E.; Laurent, S.; et al. 2007 ESH-ESC Practice Guidelines for the Management of Arterial Hypertension. *J. Hypertens.* **2007**, *25*, 1751–1762. [CrossRef]
6. Ramnarine, K.V.; Garrard, J.W.; Dexter, K.; Nduwayo, S.; Panerai, R.B.; Robinson, T.G. Shear Wave Elastography Assessment of Carotid Plaque Stiffness: In Vitro Reproducibility Study. *Ultrasound Med. Biol.* **2014**, *40*, 200–209. [CrossRef]
7. Couade, M.; Pernot, M.; Prada, C.; Messas, E.; Emmerich, J.; Bruneval, P.; Criton, A.; Fink, M.; Tanter, M. Quantitative Assessment of Arterial Wall Biomechanical Properties Using Shear Wave Imaging. *Ultrasound Med. Boil.* **2010**, *36*, 1662–1676. [CrossRef]
8. Luo, J.; Li, R.X.; Konofagou, E.E. Pulse wave imaging of the human carotid artery: An in vivo feasibility study. *IEEE Trans. Ultrason. Ferroelectr. Freq. Control* **2012**, *59*, 174–181. [CrossRef]
9. American College of Cardiology Foundation/American Heart Association Task Force. Guideline on the Management of Patients with Extracranial Carotid and Vertebral Artery Disease: Executive Summary. *J. Am. Coll. Cardiol.* **2011**, *57*, 1002–1044. [CrossRef] [PubMed]
10. Vappou, J.; Luo, J.; Okajima, K.; Di Tullio, M.; Konofagou, E. Aortic Pulse Wave Velocity Measured by Pulse Wave Imaging (Pwi): A Comparison with Applanation Tonometry. *Artery Res.* **2011**, *5*, 65–71. [CrossRef] [PubMed]
11. Vappou, J.; Luo, J.; Konofagou, E.E. Pulse Wave Imaging for Noninvasive and Quantitative Measurement of Arterial Stiffness In Vivo. *Am. J. Hypertens.* **2010**, *23*, 393–398. [CrossRef] [PubMed]
12. Luo, J.; Fujikura, K.; Tyrie, L.; Tilson, M.; Konofagou, E. Pulse Wave Imaging of Normal and Aneurysmal Abdominal Aortas in Vivo. *IEEE Trans. Med. Imaging* **2008**, *28*, 477–486.
13. Apostolakis, I.-Z.; Nauleau, P.; Papadacci, C.; McGarry, M.D.; Konofagou, E.E. Feasibility and Validation of 4-D Pulse Wave Imaging in Phantoms Andin Vivo. *IEEE Trans. Ultrason. Ferroelectr. Freq. Control* **2017**, *64*, 1305–1317. [CrossRef] [PubMed]

14. Li, H.; Chayer, B.; Cardinal, M.-H.R.; Muijsers, J.; Van Den Hoven, M.; Qin, Z.; Gesnik, M.; Soulez, G.; Lopata, R.G.P.; Cloutier, G. Investigation of out-of-Plane Motion Artifacts in 2d Noninvasive Vascular Ultrasound Elastography. *Phys. Med. Biol.* **2018**, *63*, 245003. [CrossRef] [PubMed]
15. FFenster, A.; Downey, D.B.; Cardinal, H.N. Three-Dimensional Ultrasound Imaging. *Phys. Med. Biol.* **2001**, *46*, R67–R99. [CrossRef] [PubMed]
16. Holbek, S.; Pihl, M.J.; Ewertsen, C.; Nielsen, M.B.; Jensen, J.A. In Vivo 3-D Vector Velocity Estimation with Continuous Data. In Proceedings of the 2015 IEEE International Ultrasonics Symposium, Taipei, Taiwan, 21–24 October 2015.
17. Harloff, A. Carotid Plaque Hemodynamics. *Interv. Neurol.* **2012**, *1*, 44–54. [CrossRef]
18. Huang, Q.; Zeng, Z. A Review on Real-Time 3d Ultrasound Imaging Technology. *BioMed Res. Int.* **2017**, *2017*, 1–20. [CrossRef]
19. Downey, D.B.; Fenster, A. Vascular Imaging with a Three-Dimensional Power Doppler System. *Am. J. Roentgenol.* **1995**, *165*, 665–668. [CrossRef]
20. Picot, P.A.; Rickey, D.W.; Mitchell, R.; Rankin, R.N.; Fenster, A. Three-Dimensional Colour Doppler Imaging. *Ultrasound Med. Boil.* **1993**, *19*, 95–104. [CrossRef]
21. Gao, H.; Huang, Q.; Xu, X.; Li, X. Wireless and Sensorless 3D Ultrasound Imaging. *Neurocomputing* **2016**, *195*, 159–171. [CrossRef]
22. Welch, J.; Johnson, J.; Bax, M.; Badr, R.; Shahidi, R. A Real-Time Freehand 3D Ultrasound System for Image-Guided Surgery. In Proceedings of the 2000 IEEE International Ultrasonics Symposium, San Juan, Puerto Rico, 22–25 October 2000.
23. Soozande, M.; Fool, F.; Shabanimotlagh, M.; Pertijs, M.; Verweij, M.; Vos, H.J.; Bosch, J.G.; De Jong, N. Virtually Extended Array Imaging Improves Lateral Resolution in High Frame Rate Volumetric Imaging. In Proceedings of the 2018 IEEE International Ultrasonics Symposium, Kobe, Japan, 22–25 October 2018.
24. Szabo, T.L. *Diagnostic Ultrasound Imaging: Inside out*; Academic Press: Cambridge, MA, USA, 2004.
25. Erikson, K.; Hairston, A.; Nicoli, A.; Stockwell, J.; White, T. A128 X128 (16k) Ultrasonic Transducer Hybrid Array. In *Acoustical Imaging*; Springer: Boston, MA, USA, 1997; pp. 485–494.
26. Chen, C.; Chen, Z.; Bera, D.; Raghunathan, S.B.; Shabanimotlagh, M.; Noothout, E.; Chang, Z.-Y.; Ponte, J.; Prins, C.; Vos, H.J. A Front-End Asic with Receive Sub-Array Beamforming Integrated with a 32 × 32 Pzt Matrix Transducer for 3-D Transesophageal Echocardiography. *IEEE J. Solid-State Circuits* **2017**, *52*, 994–1006. [CrossRef]
27. Wygant, I.O.; Jamal, N.S.; Lee, H.J.; Nikoozadeh, A.; Oralkan, O.; Karaman, M.; Khuri-Yakub, B.T. An Integrated Circuit with Transmit Beamforming Flip-Chip Bonded to a 2-D Cmut Array for 3-D Ultrasound Imaging. *IEEE Trans. Ultrason. Ferroelectr. Freq. Control* **2009**, *56*, 2145–2156. [CrossRef] [PubMed]
28. Gil Kang, H.; Bae, S.; Kim, P.; Park, J.; Lee, G.; Jung, W.; Park, M.; Kim, K.; Lee, W.; Song, T.-K.; et al. Column-Based Micro-Beamformer for Improved 2D Beamforming Using a Matrix Array Transducer. In Proceedings of the 2015 IEEE Biomedical Circuits and Systems Conference, Atlanta, GA, USA, 22–24 October 2015.
29. Santos, P.; Haugen, G.U.; Lovstakken, L.; Samset, E.; D'Hooge, J. Diverging Wave Volumetric Imaging Using Subaperture Beamforming. *IEEE Trans. Ultrason. Ferroelectr. Freq. Control* **2016**, *63*, 2114–2124. [CrossRef] [PubMed]
30. Rasmussen, M.F.; Jensen, J.A. 3-D Ultrasound Imaging Performance of a Row-Column Addressed 2-D Array Transducer: A Measurement Study. Proceeding of the 2013 IEEE International Ultrasonics Symposium, Prague, Czech Republic, 21–25 July 2013.
31. Flesch, M.; Pernot, M.; Provost, J.; Ferin, G.; Nguyen-Dinh, A.; Tanter, M.; Deffieux, T. 4d in Vivo Ultrafast Ultrasound Imaging Using a Row-Column Addressed Matrix and Coherently-Compounded Orthogonal Plane Waves. *Phys. Med. Biol.* **2017**, *62*, 4571. [CrossRef]
32. Chen, K.; Lee, H.-S.; Sodini, C.G. A Column-Row-Parallel Asic Architecture for 3d Wearable/Portable Medical Ultrasonic Imaging. In Proceedings of the 2014 Symposium on VLSI Circuits, Honolulu, HI, USA, 10–13 June 2014.
33. Savord, B.; Solomon, R. Fully Sampled Matrix Transducer for Real Time 3D Ultrasonic Imaging. In Proceedings of the 2013 IEEE Symposium on Ultrasonics, Prague, Czech Republic, 21–25 July 2013.

34. Kang, E.; Ding, Q.; Shabanimotlagh, M.; Kruizinga, P.; Chang, Z.-Y.; Noothout, E.; Vos, H.J.; Bosch, J.G.; Verweij, M.D.; De Jong, N. A Reconfigurable Ultrasound Transceiver Asic with 24 × 40 Elements for 3-D Carotid Artery Imaging. *IEEE J. Solid-State Circuits* **2018**, *53*, 2065–2075. [CrossRef]
35. Couade, M.; Pernot, M.; Messas, E.; Emmerich, J.; Hagège, A.; Fink, M.; Tanter, M. Ultrafast Imaging of the Arterial Pulse Wave. *IRBM* **2011**, *32*, 106–108. [CrossRef]
36. Hasegawa, H.; Hongo, K.; Kanai, H. Measurement of Regional Pulse Wave Velocity Using Very High Frame Rate Ultrasound. *J. Med. Ultrason.* **2012**, *40*, 91–98. [CrossRef]
37. Hansen, F.; Mangell, P.; Sonesson, B.; Länne, T. Diameter and Compliance in the Human Common Carotid Artery—Variations with Age and Sex. *Ultrasound Med. Biol.* **1995**, *21*, 1–9. [CrossRef]
38. Jensen, J.A. Field: A Program for Simulating Ultrasound Systems. In Proceedings of the 10th Nordic Baltic Conference on Biomedical Imaging, Tampere, Finland, 9–13 June 1996; Volume 4, pp. 351–353.
39. Jensen, J.A.; Svendsen, N. Calculation of Pressure Fields from Arbitrarily Shaped, Apodized, and Excited Ultrasound Transducers. *IEEE Trans. Ultrason. Ferroelectr. Freq. Control* **1992**, *39*, 262–267. [CrossRef]
40. Hasegawa, H.; Kanai, H. Effect of Element Directivity on Adaptive Beamforming Applied to High-Frame-Rate Ultrasound. *IEEE Trans. Ultrason. Ferroelectr. Freq. Control* **2015**, *62*, 511–523. [CrossRef]
41. Hergum, T.; Bjastad, T.; Kristoffersen, K.; Torp, H. Parallel Beamforming Using Synthetic Transmit Beams. *IEEE Trans. Ultrason. Ferroelectr. Freq. Control* **2007**, *54*, 271–280. [CrossRef] [PubMed]
42. Stepinski, T. An Implementation of Synthetic Aperture Focusing Technique in Frequency Domain. *IEEE Trans. Ultrason. Ferroelectr. Freq. Control* **2007**, *54*, 1399–1408. [CrossRef] [PubMed]
43. Jing, W.; Jian-Yu, L. Motion Artifacts of Extended High Frame Rate Imaging. *IEEE Trans. Ultrason. Ferroelectr. Freq. Control* **2007**, *54*, 1303–1315. [CrossRef] [PubMed]
44. Matrone, G.; Savoia, A.S.; Caliano, G.; Magenes, G. The Delay Multiply and Sum Beamforming Algorithm in Ultrasound B-Mode Medical Imaging. *IEEE Trans. Med. Imaging* **2014**, *34*, 940–949. [CrossRef] [PubMed]
45. Mozaffarzadeh, M.; Sadeghi, M.; Mahloojifar, A.; Orooji, M. Double-Stage Delay Multiply and Sum Beamforming Algorithm Applied to Ultrasound Medical Imaging. *Ultrasound Med. Biol.* **2018**, *44*, 677–686. [CrossRef] [PubMed]
46. Mozaffarzadeh, M.; Mahloojifar, A.; Orooji, M.; Adabi, S.; Nasiriavanaki, M. Double-Stage Delay Multiply and Sum Beamforming Algorithm: Application to Linear-Array Photoacoustic Imaging. *IEEE Trans. Biomed. Eng.* **2018**, *65*, 31–42. [CrossRef]
47. KKortbek, J.; Jensen, J.A.; Gammelmark, K.L. Sequential Beamforming for Synthetic Aperture Imaging. *Ultrasonics* **2013**, *53*, 1–16. [CrossRef]
48. Matrone, G.; Lashkevich, E.; Bertoni, A.; Ramalli, A.; Savoia, A.S.; Magenes, G. Effects of Coherence-Based Beamforming on Breast Ultrasound Elastograms. In Proceedings of the 2019 IEEE International Ultrasonics Symposium, Glasgow, UK, 6–9 October 2019.